Bulletin of the Seismological Society of America. Vol. 58, No. 1, pp. 179–214. February, 1968

THE CRUST-MANTLE TRANSITION IN THE BERING SEA

By Donald V. Helmberger

ABSTRACT

A plane layered oceanic crustal model is investigated. A point source and receiver are located in the oceanic fluid layer. The Mohorovičić discontinuity is treated as a layered transition zone. De Hoop's modification of Cagniard's method is used to obtain the exact transient response which is convolved with the source pulse shape and the instrumental system function to yield theoretical seismograms.

When the boundary is an interface or a thin layered transition zone the head wave is a small pure refraction which is followed by a strong reflection. As the transition zone grows in thickness the head wave receives both refracted and reflected energy and becomes the dominant feature. These results compare favorably with observations made in the Bering Sea.

This study suggests that the transition zone is thin, probably less than 1 km, in the Northern Aleutian Basin. Southward approaching the Aleutian Islands the transition zone thickens so that no major discontinuity exists between the crust and mantle.

Introduction

In recent years a large number of investigations have been made concerning the structure of the oceanic crust. Many of these have utilized the travel times of seismic waves produced by explosives. Recently, Červeny (1965) made an interesting observation. While studying seismic arrivals in the Northern Pacific from the crust-mantle (Moho) transition, he noticed that a strong event arriving after the Moho refraction could be interpreted as a Moho reflection. He also points out that this event is missing in other regions. Oceanic seismic records are presented in Figure 1 to illustrate the phenomenon.

It is probable that the sharpness of the Moho transition is the determining factor. Investigating this effect will be one of the principal aims of this study. In this investigation we will produce synthetic seismograms of the first 1.5 seconds of record after the onset of motion. This will allow comparisons to be made between seismic models and observations.

The crustal model that will be considered is made up of plane, homogeneous, isotropic layers. A point source of pressure and the pressure receiver are located in a fluid layer, the ocean. The fluid layer rests on a stack of solid layers, the final layer having no lower boundary. Cylindrical coordinates are used with z increasing upward from the bottom of the fluid and r the horizontal coordinate. The source is located at $r = 0$, $z = h$. No angular dependence will be allowed. We assume the layered media to be perfectly elastic, such that the usual wave equations apply. Gravitational effects are excluded in the wave equations.

The problem can be simplified if the fluid layer is replaced by a fluid half space. This can be accomplished by making the following assumptions and limitations.

The surface reflections are treated as mirror images and are replaced by fictitious sources. The geometry is limited to h and z being much larger than d_i where d_1 is the distance from the surface to source and d_2 is the distance from the surface to receiver. By allowing energy paths which have small travel times compared to water transmitted paths, only two images need be considered. Furthermore, for $d_i \ll h$ or z the ray paths can be assumed identical. Knowing the response in the fluid half space will allow the construction of the solution for the fluid layer by just adding up the half space response with the proper lags.

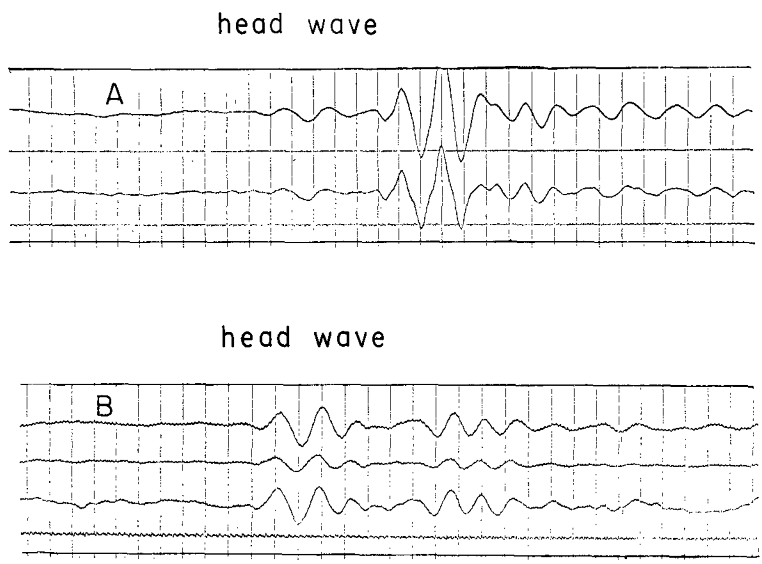

FIG. 1. Observations from the Bering Sea: (A) Northern Aleutian Basin, range 78 km, showing weak head wave followed by strong reflection, and (B) Southern Aleutian Basin, range 84 km, showing strong head wave. The timing lines are spaced every one tenth of a second.

Unfortunately, we will not be able to use the usual asymptotic solution to the wave equations as developed by Jeffreys (1926). The reason is that the refracted and reflected events are not sufficiently separated in time to make the asymptotic theory valid. However, it is possible to solve the wave equations involved exactly by applying the Cagniard method. Actually the method originated with Lamb (1904) and was later generalized by Cagniard (1939). Pekeris and his associates have applied the method to many problems. The most recent, by Pekeris, Alterman, Abramovici and Jarosch (1965), applies to the case of a solid layer overlying a solid half space. The procedure that we will follow is a version modified by de Hoop (1960) and, later, by Gilbert (1963). The modified version allows the line source theory developed by Gilbert and Knopoff (1961) to be used with only minor changes.

Multi-Layer Problem

The objective of this section is to provide a method for determining the pressure response in a fluid half space overlying a stratified solid half space. Applying the method of generalized reflection and transmission coefficients, Weyl (1919) and

Spencer (1960), it is possible to construct an integral representation for a disturbance which has traversed the strata in some specified mode of propagation. However, to be useful these solutions must not involve too many generalized rays. The simplest models are, therefore, models containing thick layers so that only a few rays arrive at the receiver in the first 1.5 seconds of recording. We will now consider such a model where no internal reflections are required; also no shear paths will be needed. The model is given in Figure 2.

Let P be the pressure with r the horizontal coordinate and z increasing upward. The Laplace transform with respect to time is denoted by an overbar. The point

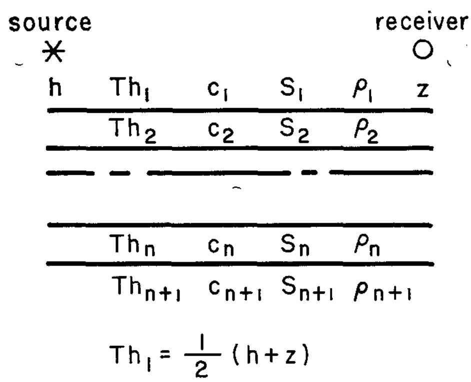

FIG. 2. Oceanic crustal model.

source emits a step function of unit strength located at $r = 0$, $z = h$. Then the integral expression for the transformed response from the bottom of the nth layer is

$$\bar{P}(r, z, s) = \frac{2}{\pi} \mathcal{I}\mathrm{m} \int_0^{i\infty} K_0(spr) e^{-sg(p)} \frac{p}{\eta_1} \mathcal{R}(p) \mathcal{T}(p) \, dp \tag{1}$$

where

$$g(p) \equiv \sum_{j=1}^{n} Th_j \eta_j \tag{2}$$

$$\mathcal{T}(p) \equiv T_{12} \cdot T_{23} \cdots T_{n-1,n} \cdot T_{n,n-1} \cdots T_{21} \tag{3}$$

$$\mathcal{R}(p) \equiv \text{Reflection coefficient at } n, n + 1 \tag{4}$$

$$\eta_j \equiv \left(\frac{1}{c_j^2} - p^2 \right)^{1/2}.$$

The T's are the generalized transmission coefficients for the various interfaces. Equation (1) describes the response that has traveled exclusively in the P-mode and contains the reflected motion as well as the refracted if the latter exists. After some transformations which are discussed in the Appendix, $P(r, z, t)$ can be written as

$$P(r, z, t) = \frac{2}{\pi} \mathcal{I}\mathrm{m} \int^{t} \frac{p}{\eta_1} \left(\frac{dp}{d\tau}\right) \frac{\mathcal{R}(p)\mathcal{T}(p)H(t - \tau)\, d\tau}{(t - \tau)^{1/2}(t - \tau + 2pr)^{1/2}} \tag{5}$$

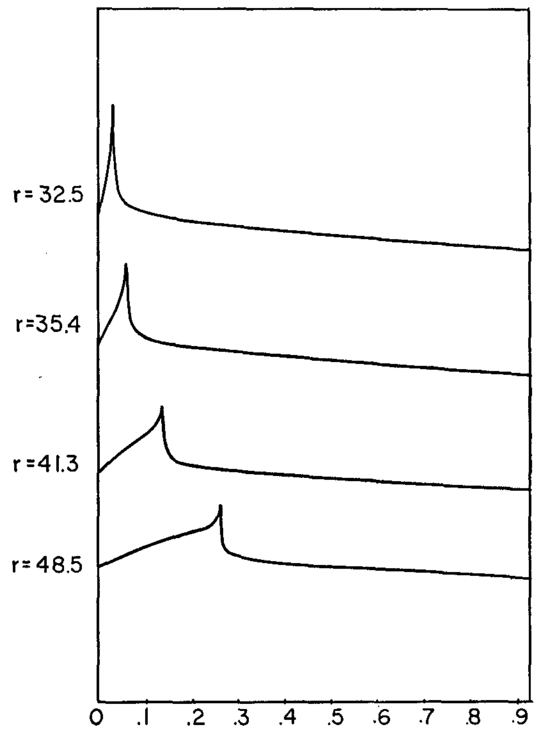

FIG. 3. Numerical solution of (5) applied to the model in Figure 8 assuming a unit step source. This includes only the response from the bottom interface. The refraction begins at $t = 0$. The strong peak in each waveform is due to the logarithmic singularity at reflection.

where

$$\tau = pr + 2\eta_j T h_j$$

$$\frac{dp}{d\tau} = \left(r - 2p \frac{Th_j}{\eta_j}\right)^{-1}.$$

The j's are to be summed from 1 to n. Since p is a function of τ the integral in (5) is just a temporal convolution and can be evaluated numerically. An example calculation for the model given in Figure 8 is presented in Figure 3. The numerical solution is obtained over four ranges starting just past the critical angle. We are assuming a step source so we expect the refraction to start as a ramp with a logarithmic singularity at reflection. These features are verified in the first motion approximations given in the Appendix. To obtain the desired synthetic waveform requires a convolution of the above pressure response with an appropriate transfer function. The transfer function contains the source and instrumentation which we now discuss.

Source Function

The general character of the pressure output produced by underwater explosives is well established. In general, underwater explosions emit a shock wave followed by a series of bubble pulses caused by an oscillating gas bubble; hence the name. Empirical pressure source functions have been tabulated by Arons (1948, 1954) where the pressure-time function is expressed as a function of charge weight and depth of shot. The bubble pulses are fairly symmetrical and are matched by an

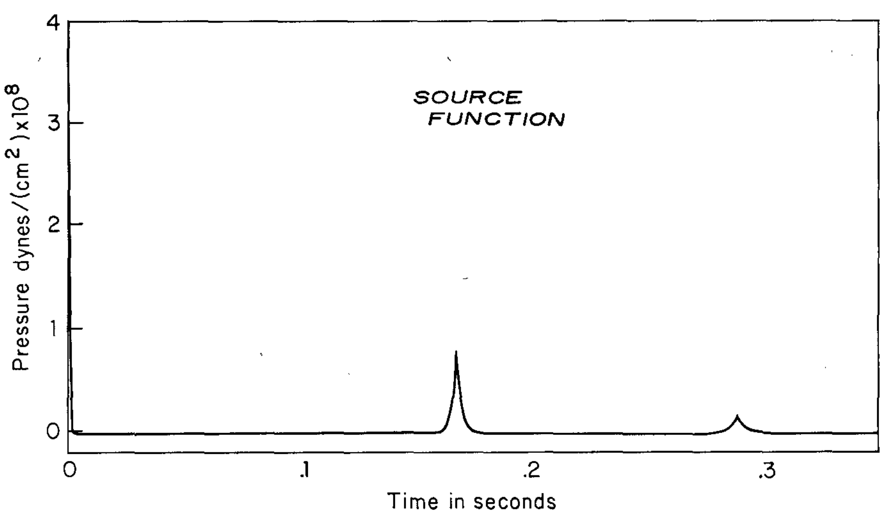

FIG. 4. Source function due to a 50 pound charge of TNT fired at a depth of 190 feet, measured at a distance of ($W_0^{1/3}/0.35$) expressed in feet where W_0 is the charge size measured in pounds.

exponential rise and decay. The shock wave is described by only an exponential decay; apparently the rise is instantaneous.

Since the pressure goes negative between pulses, a steady negative pressure is added such that the integrated pressure curve is zero. The justification of this procedure along with the empirical equations involved is discussed by Weston (1960). An example of a source function, $P_0(t)$, of the above type is given in Figure 4.

System Function

At this stage we require a description of the transfer from pressure in the water to the trace on oscillograms. This relation will be called the system function. Ideally, the oscillogram resulting from a delta-function in pressure input is desired. This prospect, unfortunately, raises some practical problems.

The system function, $I(t)$, was obtained by introducing a step of voltage into the system, simulating a step in voltage output of the hydrophone crystal. The resulting function is then differentiated producing the system response for a delta function input. The $I(t)$ resulting from a 530 μvolt input at full gain is given in Figure 5. The conversion from pressure to μvolts is obtained from the hydrophone calibration. We assume that the hydrophone crystal voltage output is proportional to pressure at the frequencies involved in our $I(t)$. This is justified because the principal frequency content of $I(t)$ is above the crystal's low frequency cut-off. The

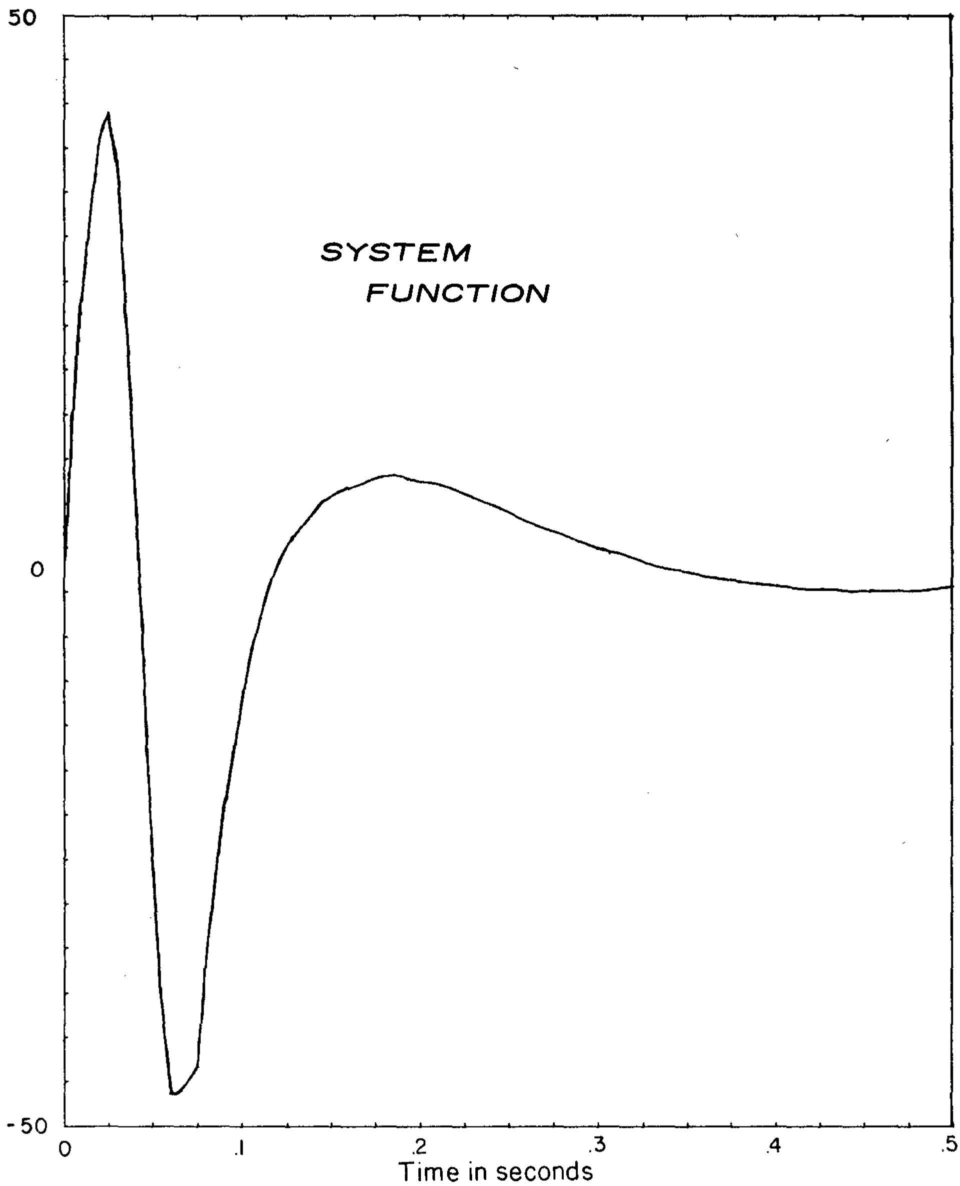

FIG. 5. The system response due to a delta function in voltage. The magnitude is expressed in decimillimeters and is the result of a voltage input of 530 μvolts.

AX58 hydrophone used here produces 100 μvolts/(dyne/cm^2). Therefore the calibration constant becomes $C_0 = 5.3$. Thus, if one convolves the $I(t)$ in Figure 5 with a source expressed in dynes/cm^2, it is necessary to multiply by C_0 for magnitude at full gain measured in decimillimeters. The equipment used in these recordings is described by Raitt (1952) and Shor (1963).

Formulation

Finally we define a transfer function

$$T(t) \equiv P_0(t) * I(t) \rightarrow \text{summation.}$$

Then it follows operationally that the

$$\text{Synthetic response} = \left[\frac{d}{dt}(T(t)) * \text{Response of model to a unit step input}\right] C$$

where

$$C = (w_0^{1/3}/0.35)1.6 \times 10^{-3}$$

and $*$ denotes the convolution operation. C contains the calibration constant and unit conversion. In this form the synthetic response is expressed in decimillimeters versus time in seconds.

Since the summation process involves the same function with lags determined by d_1 and d_2 it is possible to optimize downward energy propagation by choosing d_1 and d_2 properly. Following this suggestion, the source and receiver are placed roughly at a depth of one quarter wave length of the dominant source frequency. This means that the source image interferes constructively with the source and likewise at the receiver. Actually the receiver is fixed, as mentioned earlier, and only the charges are fired at optimum depth. The receiver is placed roughly at the proper depth for a 20 pound charge, this depth being 160 feet. As an example we will consider a 20 pound charge fired at a depth of 54 meters with the receiver at 48 meters. The resulting transfer function with the intermediate steps is given in Figure 6. Let

$$W(t) = [P_0(t) * I(t)]H(t)$$

then

$$T(t) = W(t) - W(t - t_1) - W(t - t_2) + W(t - t_3)$$

where

$$t_1 = d_1/c, \qquad t_2 = d_2/c$$

$$t_3 = t_1 + t_2, \qquad c = 1.5 \text{ km/sec.}$$

Examining this equation with t_1, t_2, and t_3 given in Figure 6 it is easy to see how enhancement occurs. Transfer functions for other charge sizes and depths used in this paper were constructed in the same fashion.

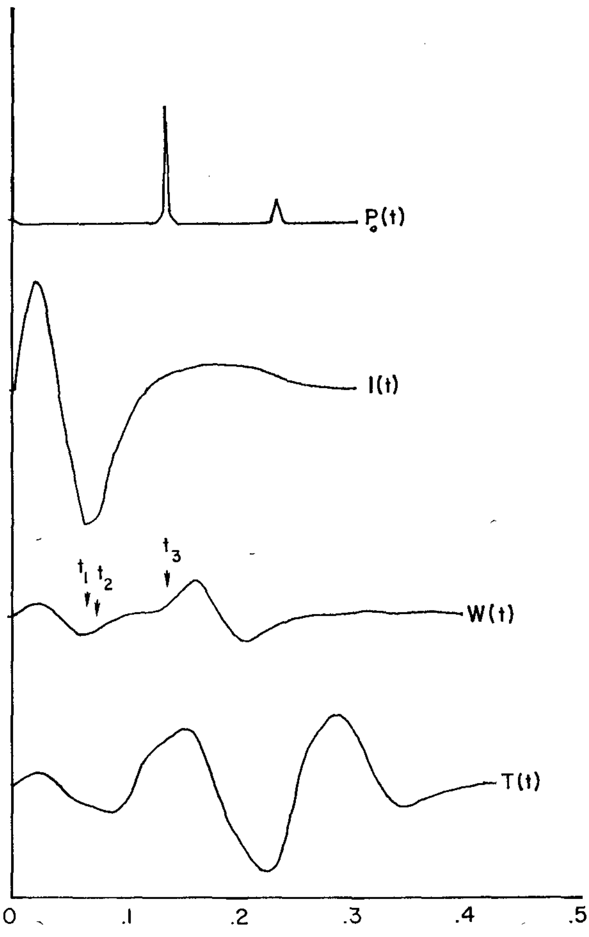

FIG. 6. This figure displays the transfer function development for a 20 pound charge fired at a depth of 160 feet. $P_0(t)$ is the source function. $I(t)$ is the system function.

NUMERICAL SOLUTIONS AND APPLICATIONS

In many oceanic regions the travel-time data from refraction studies lend themselves to layered media interpretations. We now assume such interpretations and compute synthetic waveforms to compare with observed recordings. It is advantageous to choose a region where the layers are composed of low-velocity material and are relatively thick. This allows one to construct the first 1.5 seconds of the synthetic seismogram by considering only a few generalized rays. One such area is the Aleutian Basin in the Bering Sea (see Figure 7). Since the interpretations presented earlier by Shor (1964) based on travel time data are not unique we will discover new interpretations that fit the travel-time data as well as the waveforms involved. This study suggests that the crust-mantle transition is quite sharp, probably less than a kilometer in the northeastern section and that it grows increasingly thicker southward. The phenomenon presented in Figure 1 comes from L13 (A) and L9 (B) which we will eventually produce synthetically.

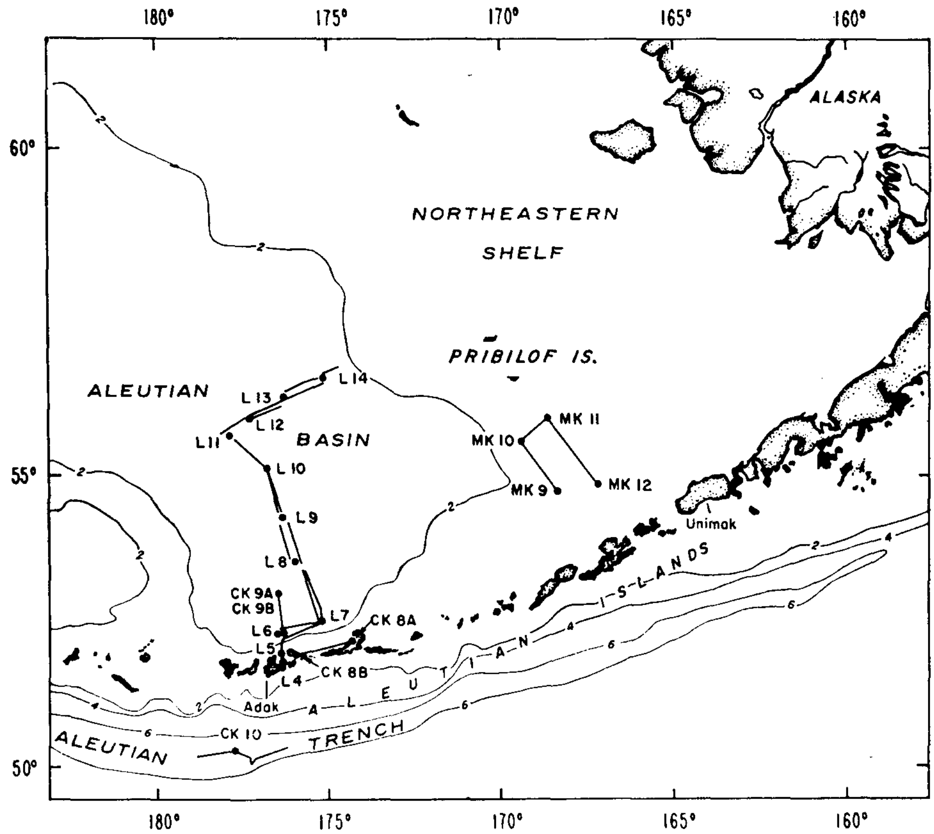

FIG. 7. Location of stations. Contour interval 2 km. (After Shor).

Oceanic crustal model for L13. The location of station L13 is given in Figure 7. This station has an incoming line as well as an outgoing line. An incoming line is defined as the seismic line produced by a shooting ship approaching the receiver, whereas an outgoing line is when the shooting ship is going away from the receiver. The incoming line will be considered here although the same model fits the outgoing line as well.

A model which fits the travel-time data for L13 is given in Figure 8. The shear velocities and densities are estimates which will be used in the theoretical treatment.

The response from the Moho for a step input for this model was presented in Figure 3. By adding the crustal response we can perform the convolutions and compare the model with observations. The comparison is given in Figure 9. Some obvious discrepancies arise. One of the most noticeable is the small amplitude of the crustal arrival. This means that the synthetic records contain mostly the interaction of the Moho reflection and its refraction. Let Δt be the difference between the reflection and refraction times. As Δt grows from 0 to 0.25 seconds the synthetic records show various degrees of interference. This is caused by the interaction of two basic periods. One is the Δt and the other is the bubble pulse interval. Both are increasing with range. For Δt larger than 0.5 seconds the two pulses separate and the first motion approximation becomes valid.

Another noticeable difference is the low energy content of the more distant

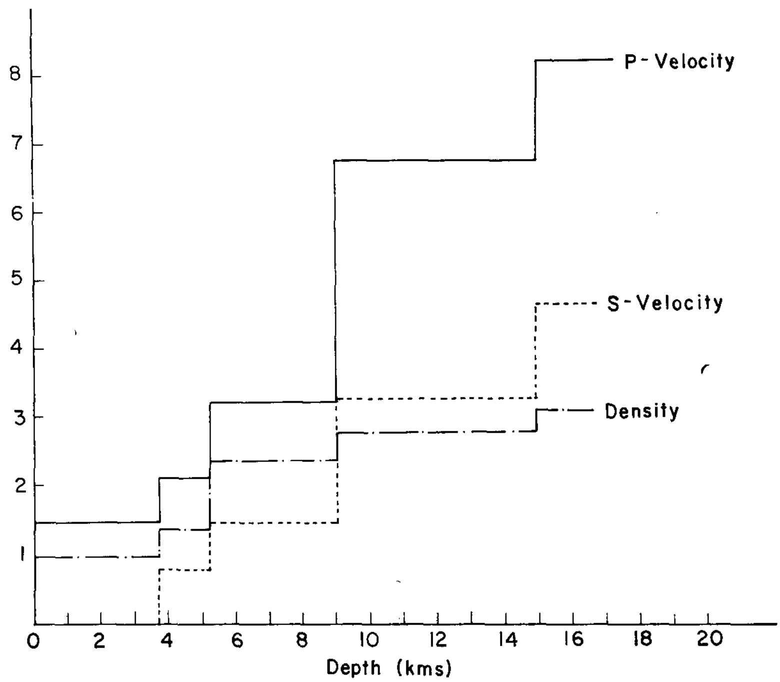

FIG. 8. Oceanic crustal model for L13. Velocities are measured in km/sec and density in gm/cm^3.

events and the excessive time interval between the refraction and reflection. This suggests that the P-wave speed should be increased in the oceanic crustal layer of the model. After some compensating travel-time changes, a new model results given in Figure 10. The new comparison is presented in Figure 11. The observations in Figure 11 have been attenuated by a factor of $\sqrt{10}$ whereas the synthetic records are reduced by 2. This discrepancy in magnitude is probably within calibration error. It also appears that the most distant shot is abnormally strong.

Transition zone. From the above discussion one gets the impression that since the reflected and refracted energy travel different paths, perhaps it is possible to gain knowledge of the lower crust from one recording. This would be the case if one were able to identify wave types. However, there is no assurance that the reflection and refraction are associated with the same interface. As we will shortly see the reflection is associated with the top of the transition zone whereas the refraction is from the upper mantle. We will now investigate such matters by looking at many models assuming a constant charge size of 50 pounds and a constant range of 75 km.

(*a*) *One layer transition.* In this section we consider the effect of adding a thin

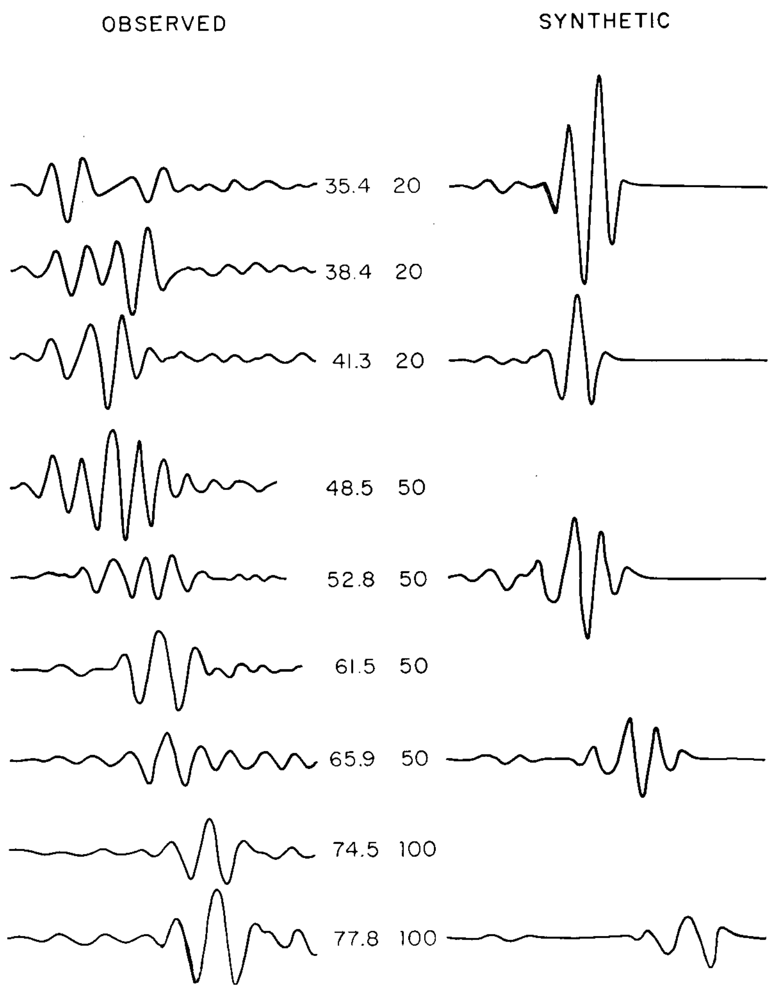

FIG. 9. Comparison of observations and synthetic responses of the model given in Figure 8. The first column of numbers gives the range in kilometers and the second gives charge size.

layer transition at the crust-mantle boundary. This necessitates ray summation involving the layer's internal reflections. The theory includes both P-mode and S-mode propagation. However, when considering distant recordings, say 75 km, the S-mode can be neglected as will be demonstrated shortly.

Suppose we consider first a model containing a 0.5 km transition layer. The parameters are given in Figure 12. The solution is obtained in a series

$$P(r, z, t) = \sum P_n(r, z, t).$$

See Appendix for details. Figure 13 displays the summation process. The response is given in Figure 14A after adding in the S-mode contribution. The S-mode contributes no noticeable effect and can be neglected at this range. A convolution of this response and a 50 pound transfer function yields Figure 14B. Interpretation of these results is straight forward. The response given in Figure 14A is exact in that no assumptions about frequency were made. Therefore, the response must give the correct answer for both high and low frequency sources. If the frequency is low the spikes are averaged out and the response looks just like the situation of no layer.

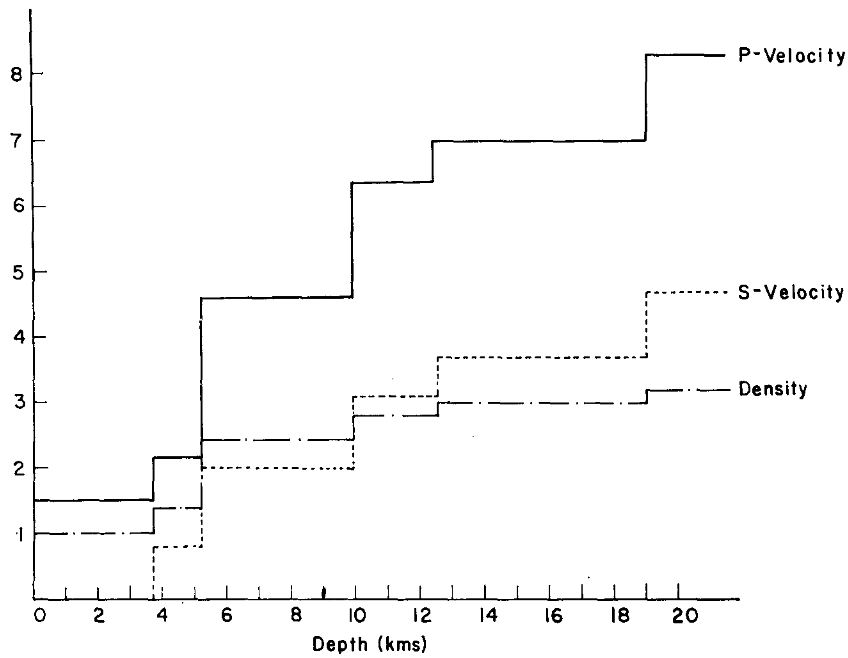

FIG. 10. Adjusted oceanic model for L13.

Looking at Figure 14B we see that our transfer function is not affected by these spikes. As the transition layer grows in thickness these spikes embrace lower frequencies.

(b) *Two layer transition.* We now consider the following two layer transition zone given in Figure 15. The solution is built up by adding the internal interactions as before, (except that only P-mode propagation will be considered). The response with the intermediate steps is presented in Figure 16. The final summation and synthetic response is given in Figure 17. The effect is to enhance the refraction relative to the reflection and bring the two waveforms together.

We now consider a model which can explain many oceanic seismic observations. Suppose the velocity increases from the top of the oceanic layer gradually into the mantle. Figure 18 contains the parameters for an approximate model. The response at 75 km and the accompanying synthetic record are given in Figure 19. This model with higher velocity transition layers has shifted the energy content of the response forward in time. Furthermore, since the transfer function averages out high frequencies, the synthetic record is not influenced much by the way the layers are introduced. After discussing L9 we will have more to say about this type of model.

Oceanic crustal model for L9. The location of station L9 (incoming) is given in Figure 7. It is approximately 300 km south of L13 which was considered earlier. Station L9 appears to fit the model just discussed in the last section, that is a model containing a gradual transition into the mantle. In that model the critical range for the bottom interface occurred at roughly 60 km. We can use this as a criterion

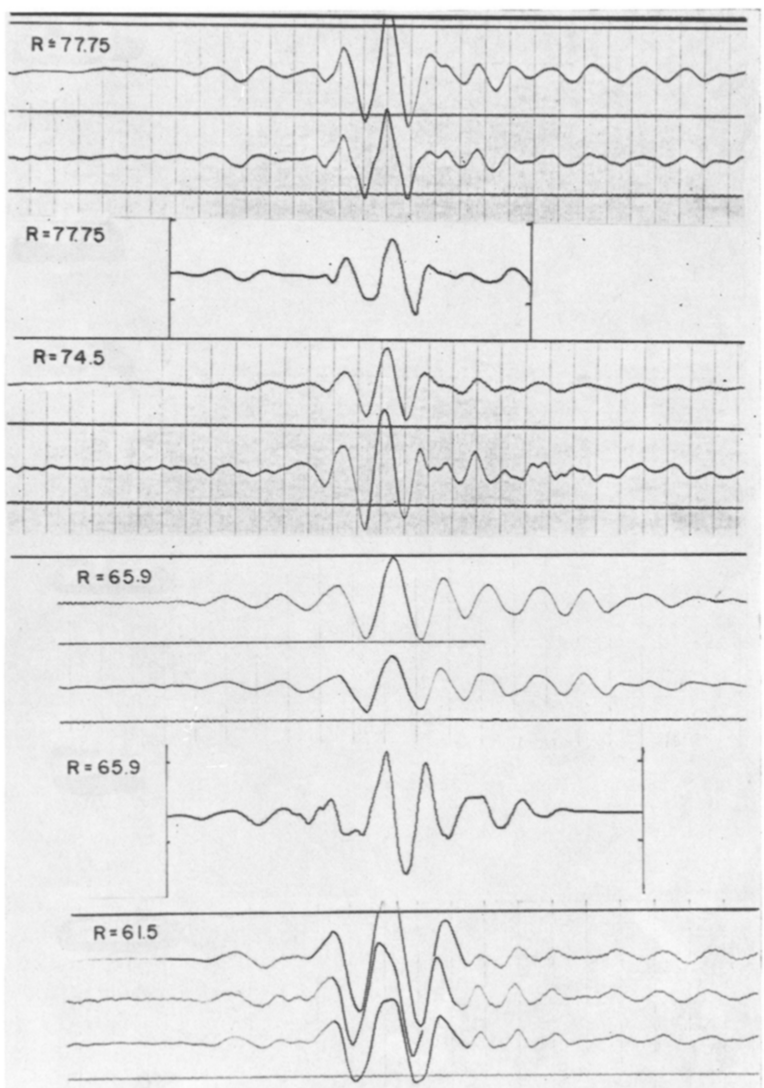

FIG. 11. Comparison of observations and synthetic waveforms based on the model given in Figure 10. The observations have been attenuated by a factor of $\sqrt{10}$ whereas the synthetic waveforms are reduced by 2. The synthetic waveforms are on the same time scale as the corresponding observation.

in adjusting the model based on the refraction data. This is accomplished by applying the following equations

$$t = pr + 2\eta_j Th_j$$

$$L = r - 2pTh_j/\eta_j .$$

At the critical angle $L = 0$ and we can use these equations to solve for any two

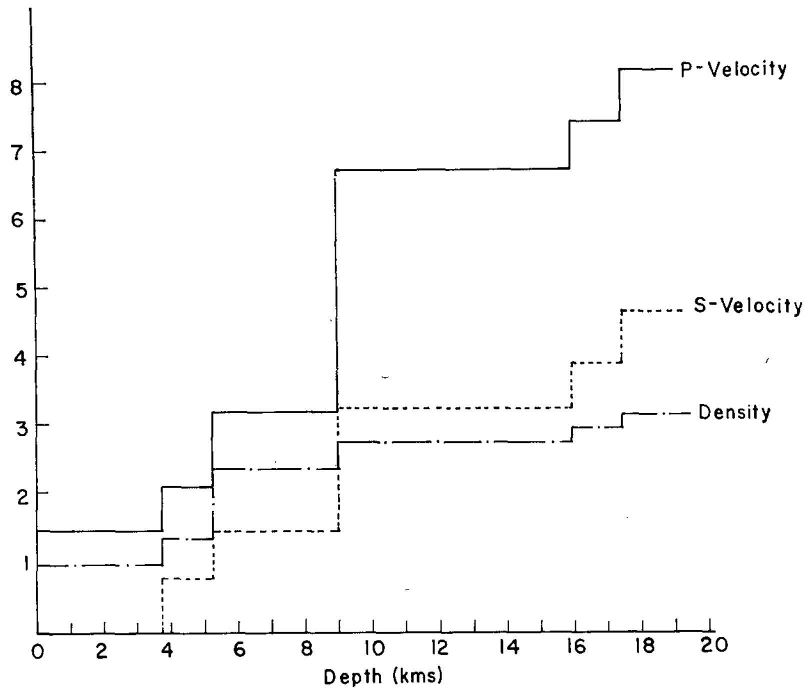

FIG. 12. Oceanic model containing transition layer.

unknowns, say c_5 and Th_5. A model which fits the travel-time data as well as this stipulation is given in Figure 20.

The summation involving the first 13 rays is given in Figure 21A. The corresponding synthetic record is shown in Figure 21B and with the two most distant observations in Figure 22. Both the observations and synthetic record are on the same magnitude scale which is attenuated by a factor of 2.5. It should be noted at this point that we have no direct measure of the mantle velocity since the data using our interpretation are dominated by reflected energy. The point is that changing the mantle velocity to 8.1 or 8.2 km/sec would not change our synthetic seismogram appreciably.

Here again the shape of our synthetic waveform is slightly different from those of the observational waveforms. This synthetic record was the first attempt at adjusting the model so, as in L13, a better one could be made by additional adjustment. For instance, it appears that the velocity 7.77 km/sec is too high because we need some interaction between the head wave and the reflection from the 6.8/7.77

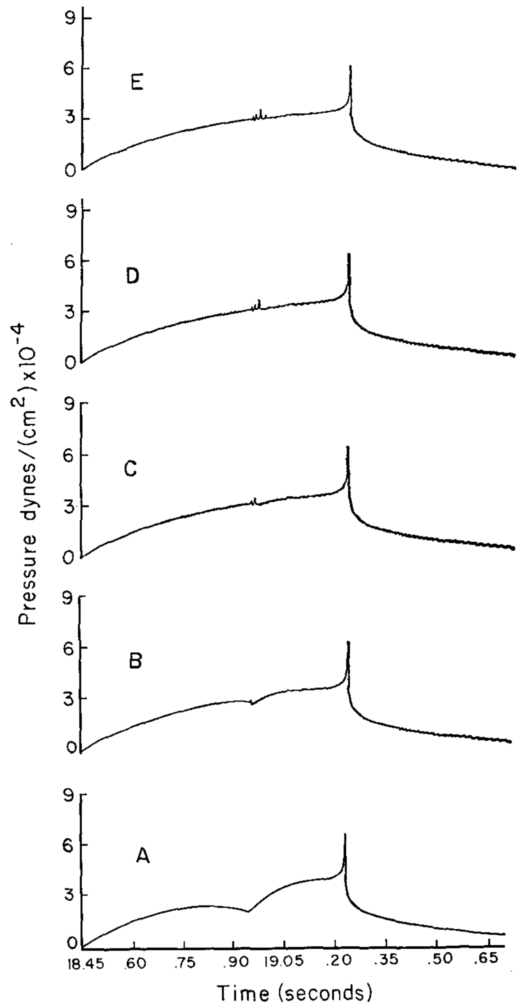

FIG. 13. Summation of generalized rays. (A) contains the responses from the bottom two interfaces. (B) also includes the first internal reflection. (C) involves two internal reflections, etc.

interface. Actually, we do not know the transfer function accurately enough to warrant a much closer match.

The observed waveforms in L9 (outgoing) are similar to those of L9 (incoming). The most distant sample of each is given in Figure 26, D and E. However, the events in L9 (outgoing) have a higher apparent velocity than those of L9 (incoming). This prompted Shor (1964) to make a dipping Moho interpretation. But since the waveform using our interpretation is constructed of reflected energy from the lower crust we would suggest that some shallow layer is thickening.

There is one other feature about this station which should be discussed. That is the decay of headwave amplitude with range. The critical range for the mantle response for this station occurs at 60 km. At the range 74 km, the refracted and reflected geometrical times are separated by only .02 seconds. This means that the head wave decays very slowly with range since the reflection is near the critical angle. The point will be more evident after the discussion given in the next section.

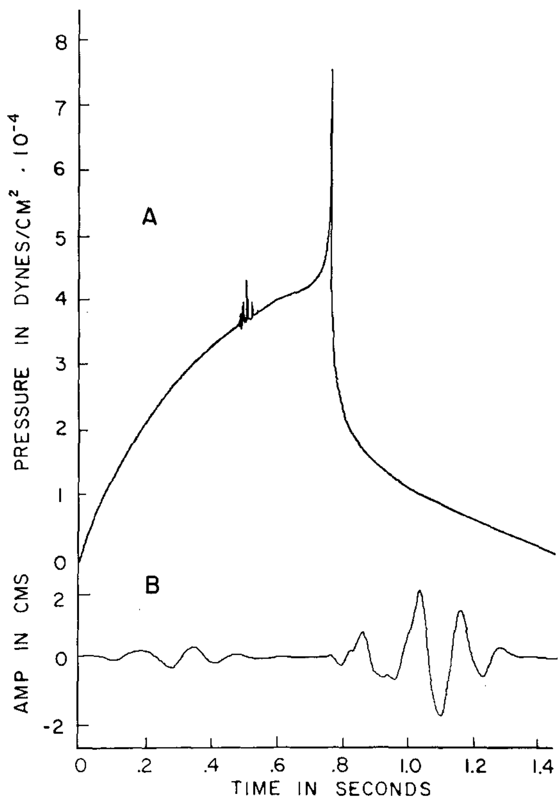

FIG. 14. Theoretical response and synthetic waveform for .5 km transition zone. (A) contains the final summation of both P and S-mode internal reflections. Waveform (B) is the synthetic response.

Prominent crustal arrivals. One of the most consistent features of the Bering Sea records is a strong crustal arrival that occurs at roughly 25 km. A set of waveforms spanning this range is given in Figure 23. This pulse has an apparent velocity of a refraction (plots as a straight line on a travel-time graph). However, its energy content is much too high according to our calibration. Besides if this is a refraction, then theory predicts a reflection at least five times stronger arriving within a second. Thus we are led to a model that allows the reflected energy to stay coupled to the refracted. The model in Figure 24 has this feature. Only the response from the bottom interface is considered. The numerical solution is given in Figure 25. In this instance, the response moves with an apparent velocity of a refraction over a range of 25 km.

Crust-mantle transition in the Aleutian Basin. It would be gratifying if one could continue the synthetic model study to all of the stations and see the vertical transition develop in the crust-mantle boundary. However, we can obtain a general impression of the lower crustal structure by looking at appropriate distant waveforms. The observations made at the greatest ranges for five lines is presented in Figure 26. The orientation of Figure 26 is northeast at the top.

After looking at the various models an interpretation is easily made as follows. The boundary between the crust and the mantle is well defined for the northern stations; that is, there is a major change in seismic velocity occurring within a thin

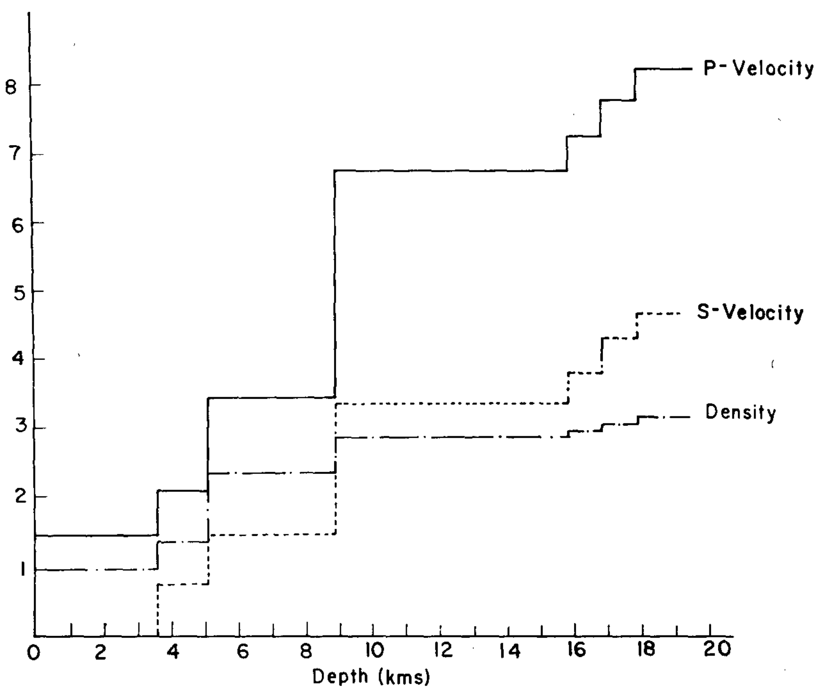

FIG. 15. Oceanic model with two layer transition.

transition zone, which is probably less than 1 km thick at L13. Southward the transition zone thickens so that at L9 no major discontinuity exists between the crust and mantle.

It should be mentioned at this point that exactly the same type of phenomenon occurs approaching the Kuril Island Arc from the concave side. That is at a distance of 500 km from the landward side of the islands Moho reflections are prominent with small head waves but approaching the islands the head waves become the prominent feature, see Tulina (1965).

SUMMARY

In this study we have attempted to explain the mechanism involved in oceanic headwave observations by computing synthetic waveforms for a number of crustal models.

Using generalized ray theory, it was possible to obtain seismic responses of models composed of homogeneous layers with plane boundaries. The transient response due to an impulsive pressure-point source was expressed in the usual form involving the integral of a Bessel function. These integrals were reduced to temporal convolutions using a technique introduced by Gilbert. The convolutions were evaluated numerically. First-motion approximations of the exact solutions produced the results as

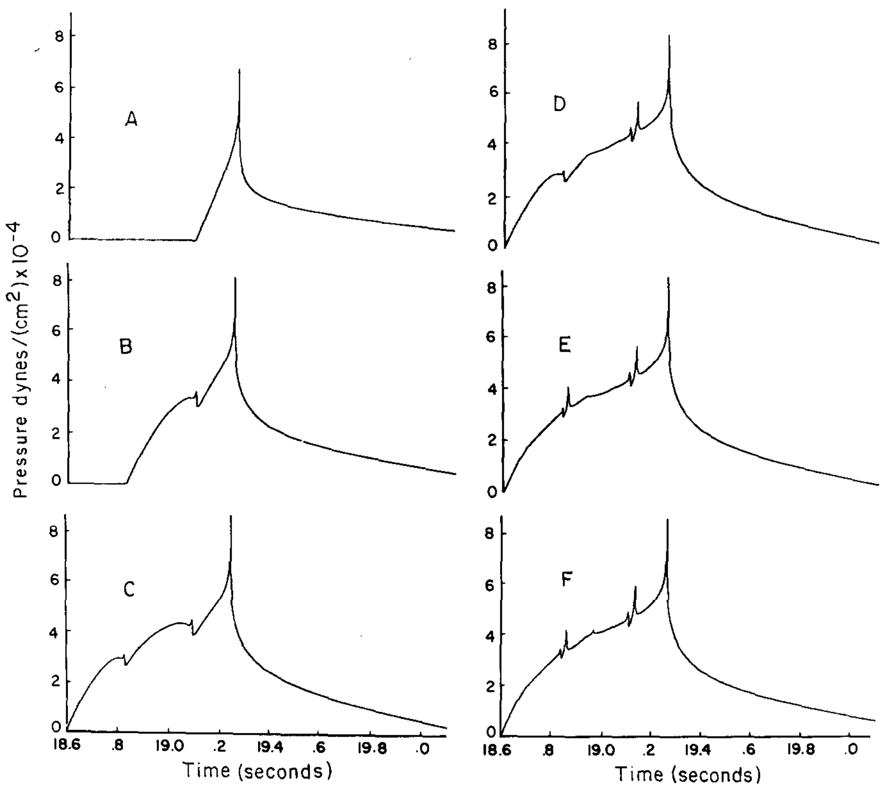

FIG. 16. Summation of generalized rays. (A) is the response from the top transitional interface. (B) includes the middle interface response. (C) also the bottom interface response. (D) includes the first internal reflection in the upper layer, etc.

follows: Assuming a delta function source the primary head wave starts as a step with a range dependence of $(rL^3)^{-1/2}$ where L is the distance traveled in the refractor. When L becomes small the step developes a spike-like shape. After the critical angle, the reflected response is that of a delta function with a simple pole singularity as a precurser.

Transfer functions containing the instrumentation, summation, and various sources were developed. These functions show the periodicity that is so common on seismograms. The periodicity is produced largely by the interaction of the bubble pulses and surface reflections.

Synthetic waveforms were produced using the transfer functions and model responses. An attempt was made at constructing models based on observations by

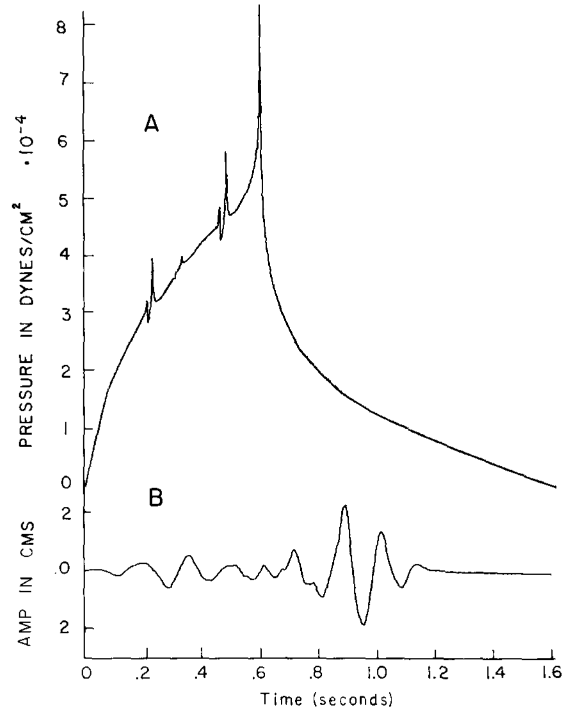

FIG. 17. Theoretical response and synthetic waveform for transition zone containing two 1 km layers. (A) contains the final summation through the second set. Waveform (B) is the synthetic response.

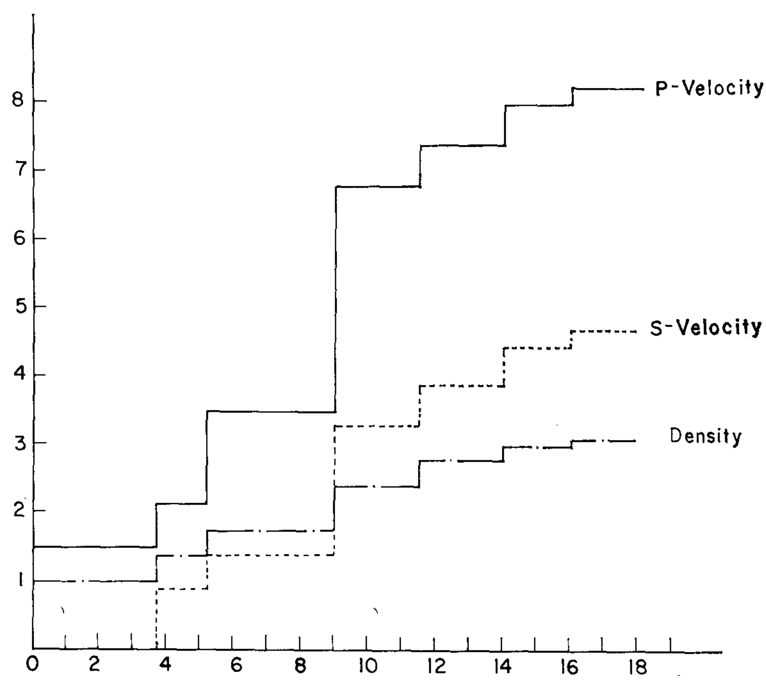

FIG. 18. Oceanic model with gradual transition from crust to mantle.

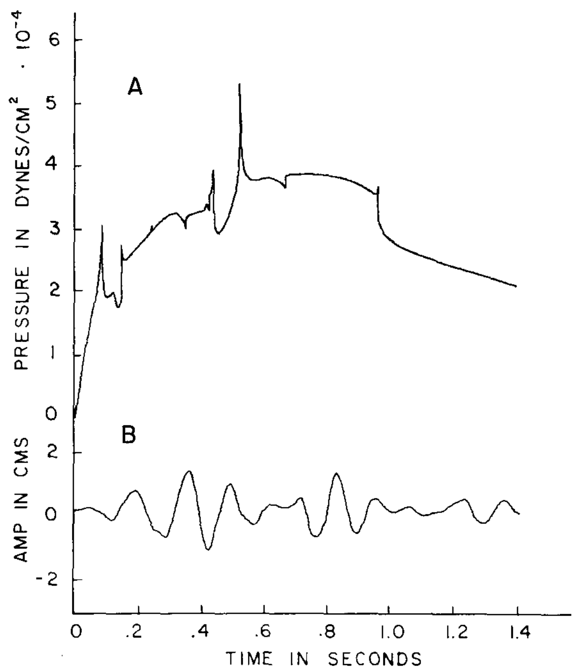

FIG. 19. Theoretical response and synthetic waveform for gradual transition. Response based on the model in Figure 18. and synthetic waveform.

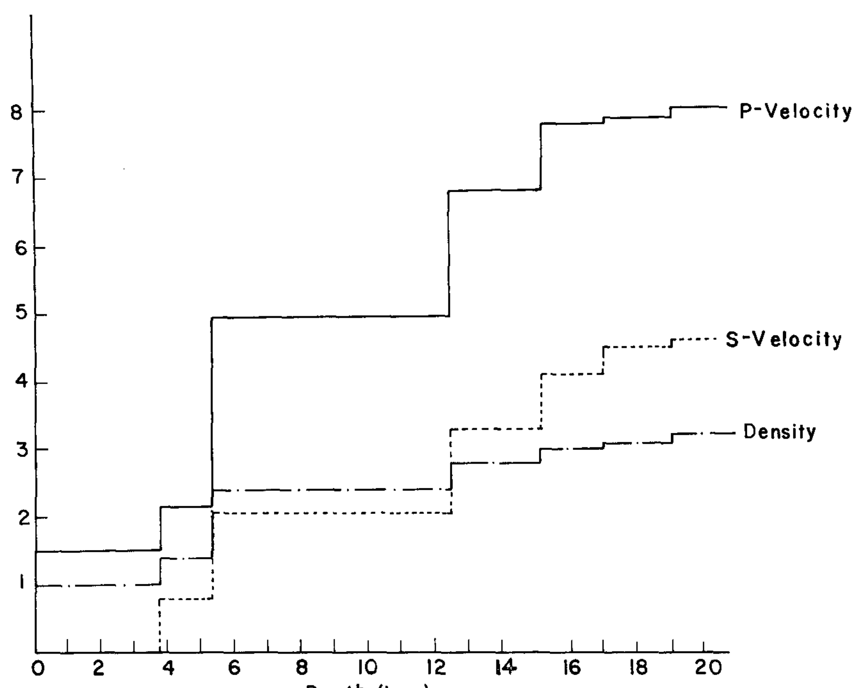

FIG. 20. Oceanic model for L9 (incoming).

constraining the models to fit travel-time data as well as the waveforms involved. This was accomplished reasonably well with two seismic stations in the Bering Sea.

The headwave observations from station L13 appear to fit a model containing a sharp velocity contrast at the crust-mantle boundary. The properties of this type of seismogram are a small headwave consisting of only refracted energy followed

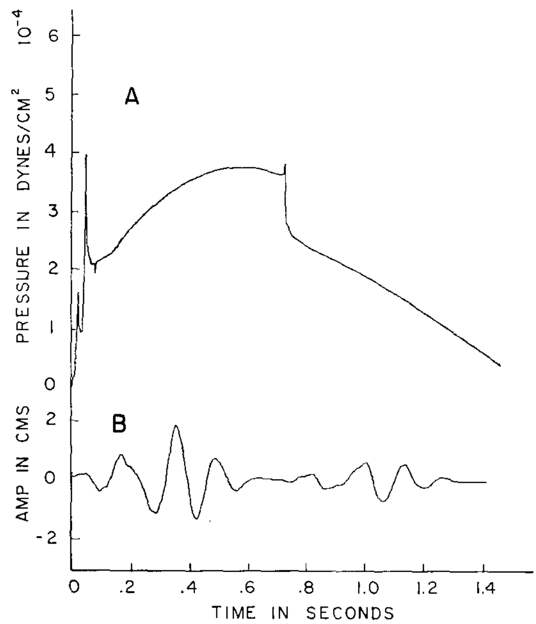

FIG. 21. Theoretical response and synthetic waveform at r = 71.1 km based on the model for L9 (incoming).

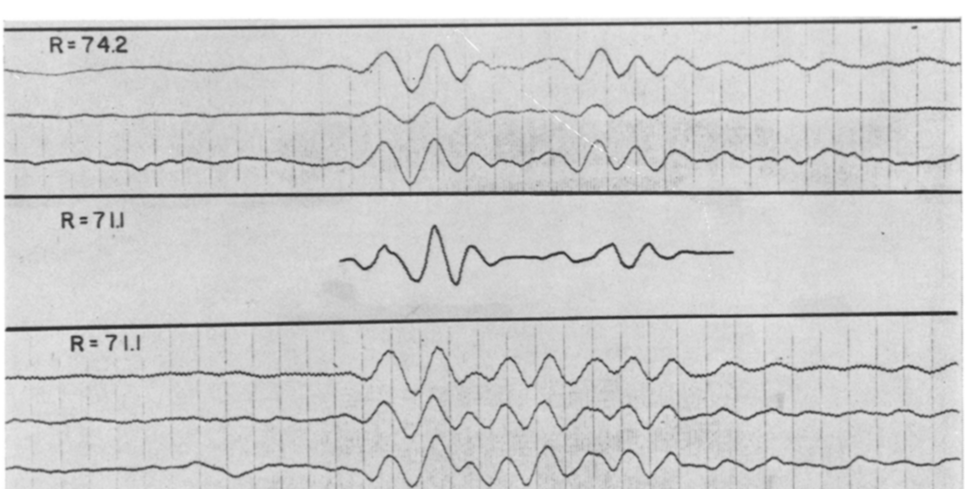

FIG. 22. Comparison between observations and synthetic waveform for L9 (incoming). The observations and synthetic waveform are reduced by a factor of 2.5.

by a dominating reflection. In this case the contrast in velocity at the Moho is high enough to allow the refraction to outrun the reflections, so that they are well separated in time. The model also predicts a rapid amplitude decay of the head wave with range.

Models with transition zones at the crust-mantle boundary show some interesting

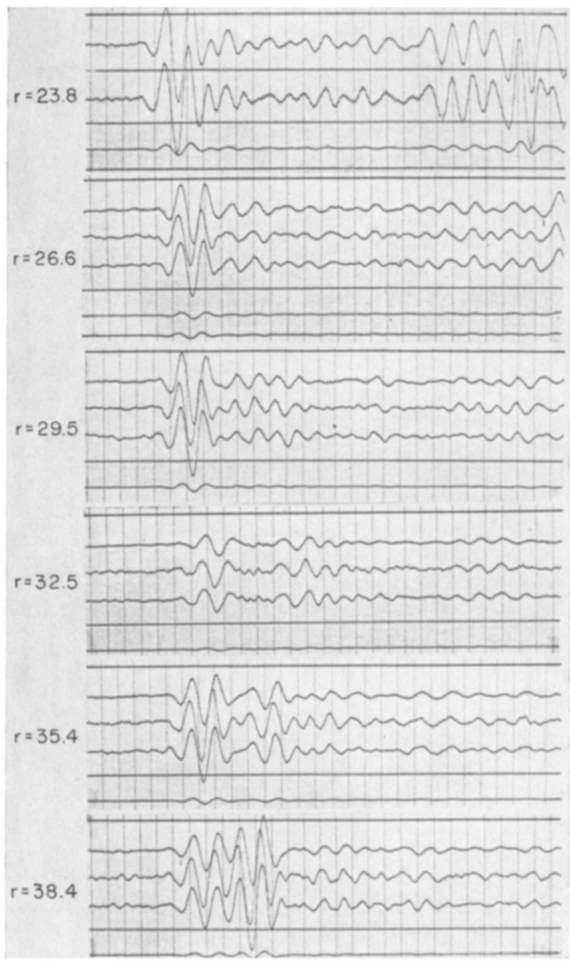

FIG. 23. Sample of a prominent crustal arrival.

results. When the transition zone is thin, less than a kilometer, the effect is to enhance the refraction because the critical angle is reached at a greater range. However, it appears impossible to distinguish this model from the earlier type using our transfer function. A model containing a gradual crust-to-mantle transition, over a 4.5 km zone, produces an entirely different type of head wave. In this case the head wave consists of both refracted and reflected energy. The reason is that the travel paths are similar since the wide angle reflected energy travels in the bottom transitional layer. Observations at station L9 appear to fit a model of this type. The synthetic waveform for this station has a strong head wave with weaker second arrivals. The head wave has a much smaller decay of amplitude with range than that of station L13.

In conclusion, we have introduced a method of computing synthetic seismograms for oceanic crustal models. By comparing observed and synthetic recordings we are able to adjust crustal models based on travel-time data to fit the waveforms involved. Thus we have a technique of extracting much more information from seismic data than conventional methods.

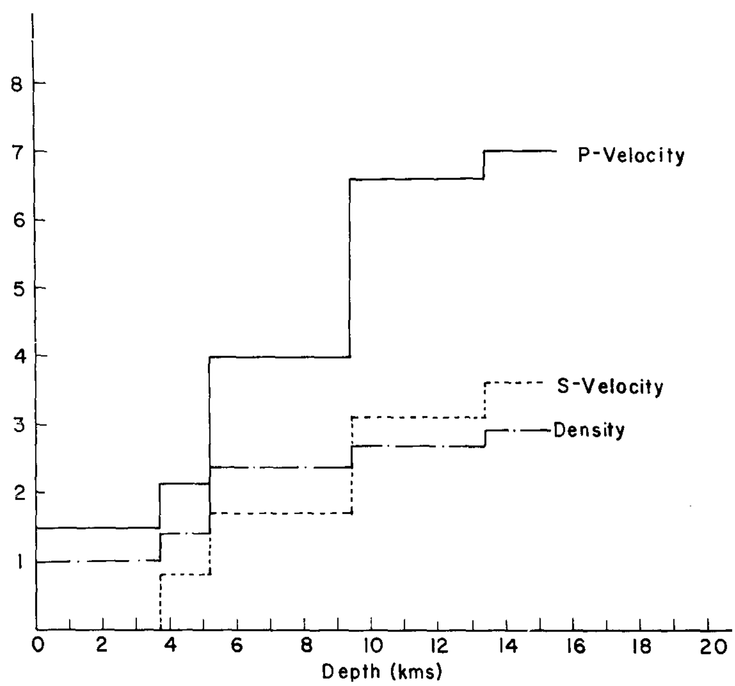

FIG. 24. Crustal model.

APPENDIX

METHOD OF ANALYSIS

The method of analysis which is applicable to layered media can also be used to solve a simpler problem, namely that of an infinite fluid. We will consider the latter problem as an introduction of the technique.

Suppose a point source emits a step function of unit strength located at $r = 0$, $z = 0$. Then the transformed pressure is

$$\bar{P}(r, z, s) = -\frac{i}{\pi} C_0 \int_\Gamma K_0(spr) e^{-s\eta_1|z|} \frac{p}{\eta_1}\, dp \tag{A1}$$

where $\eta_1 = (1/c_1^2 - p^2)^{1/2}$, c_1 = compression velocity, and Γ the path of integration, which runs along the imaginary p axis just to the right of $p = 0$. The constant C_0 has unit value with dimensions of pressure times length, which will be assumed in the following equations. The above equation was derived by Strick (1959) and others, applying the source term as a boundary condition.

The branch cut introduced by the radical η_1 runs along the real p axis starting at $p = 1/c_1$ with phase $-i$ above and $+i$ below the cut (see Figure A1). Due to the symmetry with respect to the real axis, (A1) can be rewritten

$$\bar{P}(r, z, s) = \frac{2}{\pi} \mathcal{I}\mathrm{m} \int_0^{i\infty} K_0(spr) e^{-s\eta_1 |z|} \frac{p}{\eta_1} \, dp \tag{A2}$$

where $\mathcal{I}$m indicates taking the imaginary part. The inversion of $\bar{P}(r, z, s)$ to obtain $P(r, z, t)$ is accomplished by a technique introduced by Gilbert (1963). The function

$$K_0(spr) e^{-s\eta_1 |z|}$$

is the Laplace transform of

$$\frac{H(t - pr - \eta_1 |z|)}{((t - \eta_1 |z|)^2 - p^2 r^2)^{1/2}}$$

where H is the step function. Thus the transformation back to the time domain can be achieved by operational means

$$P(r, z, t) = \frac{2}{\pi} \mathcal{I}\mathrm{m} \int_0^{i\infty} \frac{p}{\eta_1} \, dp \, \frac{H(t - pr - \eta_1 |z|)}{((t - \eta_1 |z|)^2 - p^2 r^2)^{1/2}}. \tag{A3}$$

Since the step function only has meaning when its argument is real, the contour is deformed to such a path that

$$\tau = pr + \eta_1 |z| \tag{A4}$$

is positive and real. Following de Hoop's (1960) modification of Cagniard's method (A4) gives

$$p = \frac{r}{R^2} \tau + i \frac{|z|}{R^2} (\tau^2 - R^2/c_1^2)^{1/2} \tag{A5}$$

where $R^2 = r^2 + z^2$. The new contour, Γ', is represented by (A5) for $R/c_1 < \tau < \infty$. The path follows the upper branch of a hyperbola as illustrated in Figure A1. On the Γ' contour

$$\eta_1 = \frac{|z|}{R^2} \tau - i \frac{r}{R^2} (\tau^2 - R^2/c_1^2)^{1/2}. \tag{A6}$$

Changing the variable of integration in (A3) to τ gives

$$P(r, z, t) = \frac{2}{\pi} \mathscr{I}\mathrm{m} \int_{\Gamma 1} \frac{p}{\eta_1} \left(\frac{dp}{d\tau}\right) \frac{d\tau H(t - \tau)}{(t - \tau)^{1/2}(t - \tau + 2pr)^{1/2}} \tag{A7}$$

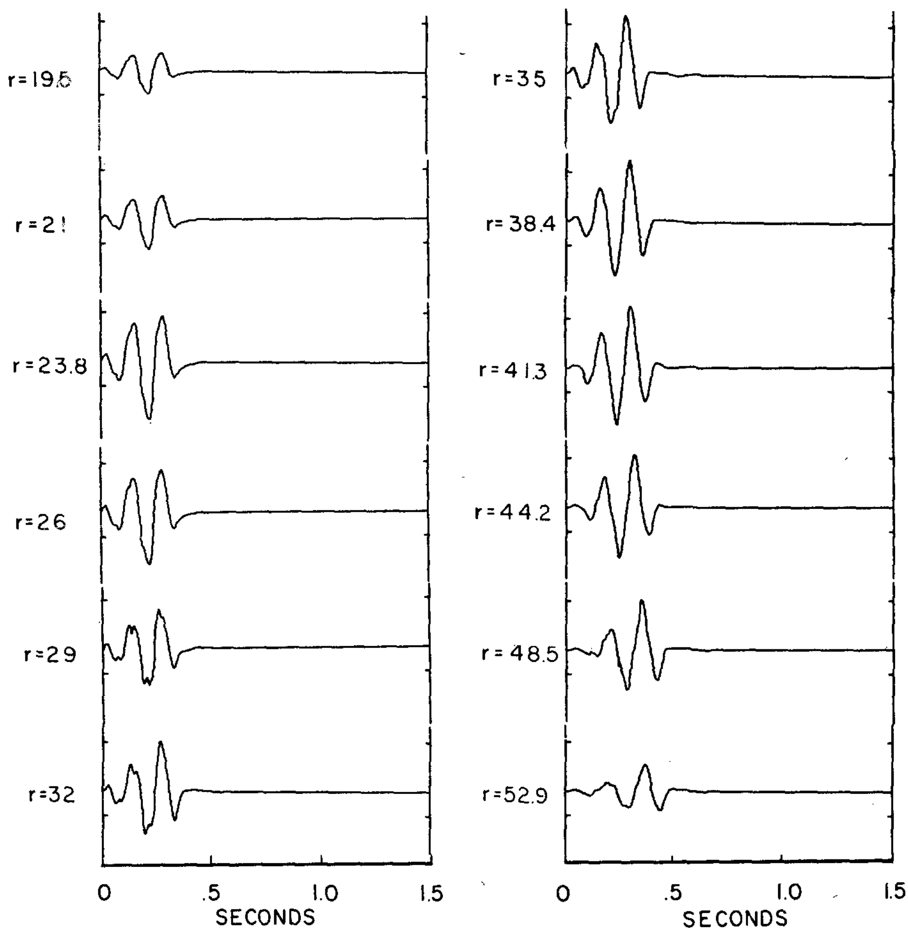

FIG. 25. Synthetic waveforms based on the crustal model of Figure 24. The critical angle occurs between $r = 26$ and $r = 29$.

where

$$\frac{dp}{d\tau} = i\eta_1 \Big/ \left(\tau^2 - \frac{R^2}{c_1^2}\right)^{1/2}.$$

Since everything in the integrand is real for $p < r/Rc_1$ that part of the integration contributes nothing. Thus (A7) can be rewritten as a temporal convolution

$$P(r, z, t) = \frac{2}{\pi} \mathscr{R}\mathrm{e} \int_{t_R}^{t} p(\tau) \left(\tau^2 - \frac{R^2}{c_1^2}\right)^{-1/2} \frac{(t - \tau)^{-1/2}\, d\tau}{(t - \tau + 2pr)^{1/2}} \tag{A8}$$

where $\Re e$ indicates the real part and $t_R = R/c_1$. Let

$$\theta = \sin^{-1}\left(\frac{t - \tau}{t - t_R}\right)^{1/2}. \tag{A9}$$

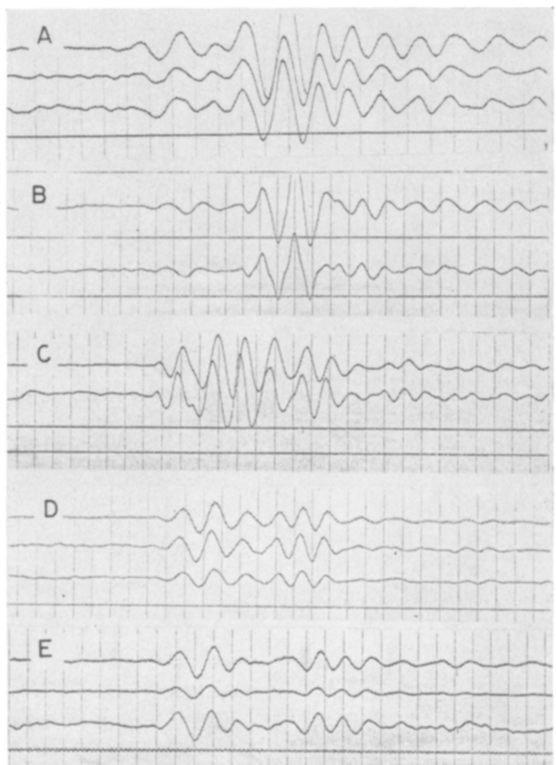

FIG. 26. Sample of head waves across the Aleutian Basin. (A) is from L13 (outgoing) at a range of 80 km. (B) is from L13 (incoming) at a range of 77.8 km. (C) is from L10 at a range of 72 km. (D) is from L9 (outgoing) at a range of 84.5 km. (E) is from L9 (incoming) at a range of 74.2 km. The gain settings are slightly higher for (A) than for the others. (B) is obtained from a 100 pound charge whereas the others involve 50 pound charges.

Then (A8) becomes

$$P(r, z, t) = \frac{4}{\pi} \Re e \int_0^{\pi/2} F(\theta)\, d\theta \tag{A10}$$

where

$$F(\theta) = \frac{p(\tau)(\tau + t_R)^{-1/2}}{(t - \tau + 2pr)^{1/2}}.$$

For $t \approx t_R$, the first-motion approximation,

$$F(\theta) \approx 1/2R \quad \text{and} \quad P(r, z, t) = \frac{1}{R} H(t - t_R). \tag{A11}$$

This result can be verified for later times by numerical integration of (A10) for each t. The solution is exactly $1/R$ as shown by Dix (1954).

We can also look upon (A10) as a parametric equation in p. Suppose we chose a set of real p's starting at $p_0 = p(t_R)$, the point where the contour leaves the real p axes. For each real value p_R corresponds an imaginary p_I satisfying (A4). Substituting this complex set into (A4) and (A10) yields $P(r, z, t)$ where the t dependence is obtained on an irregular interval.

Simple Crustal Model

Suppose we now return to (1) discussed earlier.

$$\bar{P}(r, z, s) = \frac{2}{\pi} \mathcal{I}\mathrm{m} \int_0^{i\infty} K_0(spr) e^{-sg(p)} \frac{p}{\eta} \mathcal{R}(p)\mathfrak{I}(p)\, dp. \tag{1}$$

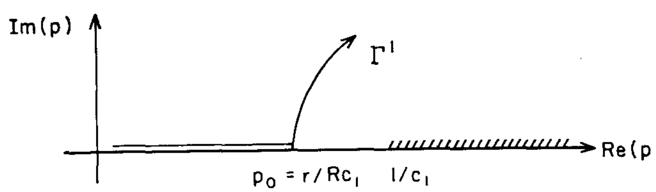

FIG. A1. First quadrant of the complex p plane showing branch cut along the real p axis.

The inversion of $\bar{P}(s)$ to obtain $P(t)$ can be performed as before. The function

$$K_0(spr)e^{-sg(p)}$$

is the Laplace transform of

$$\frac{H(t - pr - g(p))}{((t - g(p))^2 - p^2r^2)^{1/2}}.$$

Thus the contour becomes

$$\tau = pr + g(p) = pr + 2Th_j\eta_j \tag{A12}$$

where τ is positive and real. The η_j's introduce additional branch cuts along the $\mathcal{R}\mathrm{e}(p)$. It is no longer feasible to solve (A12) for p as an explicit function of τ, however treating p as a parameter is sufficient. Suppose we choose a set of real p's spanning the domain of interest. Then substituting this set into (A12) produces a set of imaginary p's since the τ's must be real. This is easily accomplished numerically. The contour in the complex p-plane is obtained allowing (5) to be treated as a temporal convolution.

$$P(r, z, t) = \frac{2}{\pi} \mathcal{I}\mathrm{m} \int^t \frac{p}{\eta_1} \left(\frac{dp}{d\tau}\right) \frac{\mathcal{R}(p)\mathfrak{I}(p)H(t - \tau)\, d\tau}{(t - \tau)^{1/2}(t - \tau + 2pr)^{1/2}} \tag{5}$$

where

$$\frac{dp}{d\tau} = (r - 2pTh_j/\eta_j)^{-1}.$$

The integral expressed in (5) is slowly varying along the contour Γ' except when $p(\tau)$ is near branch points or p_0, p_0 being the point where the contour leaves the real axis. A simple way to discover the physical significance of these points is by use of (A12). The substitution of $p = 1/c_{n+1}$ and p_0 into (A12) yields the P-refracted time and the reflected time, respectively. The so-called first motion approximations are obtained by evaluating the integral in (5) at these critical points. This will be demonstrated after discussing the exact solution.

Since the integrand of (5) is real for $p < 1/c_{n+1}$ that part of the integration contributes nothing. At $p = p_R = 1/c_{n+1}$, η_{n+1} becomes imaginary and the response begins. Substituting p_R into (A12) yields

$$t_p = r/c_{n+1} + 2Th_j\left(\frac{1}{c_{n+1}^2} + \frac{1}{c_j^2}\right)^{1/2}$$

the P-refraction time.

It is convenient to break the integration along the Γ' contour into two parts, from p_r to p_0 where the p's are real and from p_0 to some arbitrary cutoff where the p's are complex. This corresponds to dividing up the τ integration from t_p to t_R and from t_R onward, where t_R is the reflected time. Equation (5) can then be rewritten

$$P(r, z, t) = P_1(r, z, t) + P_2(r, z, t)$$

where

$$P_1(r, z, t) = \frac{2}{\pi} \mathscr{I}\mathrm{m} \int_{t_P}^{t_R} \frac{p}{\eta_1}\left(\frac{dp}{d\tau}\right) \frac{\mathcal{R}(p)\mathfrak{I}(p)(t-\tau)^{-1/2}}{(t-\tau+2pr)^{1/2}}\, d\tau$$

and

$$P_2(r, z, t) = \frac{2}{\pi} \mathscr{I}\mathrm{m} \int_{t_P}^{t_R} \frac{p}{\eta_1}\left(\frac{dp}{d\tau}\right) \frac{\mathcal{R}(p)\mathfrak{I}(p)(t-\tau)^{-1/2}}{(t-\tau+2pr)^{1/2}}\Bigg)\, d\tau \qquad t > t_R\,.$$

If $t < t_R$ only P_1 need be evaluated with the upper limit of integration changed to t.

The radical $(t - \tau)^{-1/2}$ occurring in P_1 is removed by a change of variable

$$\theta = \sin^{-1}(\tau/t)^{1/2}.$$

The response becomes

$$P_1(r, z, t) = \frac{4}{\pi}\int_{\theta_C}^{\pi/2} F(\theta)\, d\theta$$

where

$$F(\theta) = \mathscr{I}\mathrm{m}\left[\mathcal{R}(p)\mathfrak{I}(p)\,\frac{p}{\eta_1}\frac{dp}{d\tau}\right]\frac{\sqrt{\tau}}{(t-\tau+2pr)^{1/2}}$$

and

$$\theta_C = \sin^{-1} (t_p/t)^{1/2}$$

The integration is now carried out numerically by using the trapezoidal rule. We choose a set of p's spanning the interval p_r to p_0. These p's are then used along with (A12) to setup the problem in parametric form as before. We pick the p's close together when $F(\theta)$ is near a critical point.

$P_2(r, z, t)$ can be evaluated using the substitution (A9) following the same procedure as that given in the infinite fluid discussion.

High-Frequency Approximation

The pressure response for a unit delta function source is

$$P(r, z, t) = \frac{2}{\pi}\frac{d}{dt} \mathcal{I}\mathrm{m} \int^t d\tau \, \mathcal{R}(p)\mathfrak{Z}(q) \frac{p}{\eta_1}\left(\frac{dp}{d\tau}\right) \frac{(t-\tau)^{1/2}}{(t-\tau+2pr)^{1/2}} . \quad \text{(A13)}$$

In dealing with high frequency or short duration sources the following approximation is valid

$$t - \tau + 2pr \approx 2pr.$$

With this simplification (A13) can be expressed as a convolution

$$P(r, z, t) = \frac{2}{\pi}\frac{d}{dt}\left(\frac{1}{\sqrt{t}} * \psi(t)\right) \quad \text{(A14)}$$

where

$$\psi(t) = \mathcal{I}\mathrm{m}\left(\mathcal{R}(p)\mathfrak{Z}(p)\, \frac{\sqrt{p}}{\eta_1}\left(\frac{dp}{d\tau}\right) \Big/ \sqrt{2r}\right). \quad \text{(A15)}$$

By assuming a high-frequency source the convolution process, as is well known eliminates interface waves (Phinney, 1961). The responses for body waves, refracted and reflected, have been approximated by Jeffreys (1926) and others. It is found that the refracted pulse has the shape of the integral of the direct, whereas the reflected has the same shape, although perhaps with opposite polarity. These approximations can be obtained from the above theory by examining (A14) about the various p's which yield t_p and t_R respectively. It will be shown that these approximations have limited application and that the more exact theory must be used for oceanic source functions in many situations, if not most.

First Motion P-Head Wave

The only function that is not slowly varying at $p = 1/c_{n+1}$ is η_{n+1}. For convenience let $m = n + 1$. Therefore to first order $p = 1/c_m$ in all functions of

(A15) except η_m. The details of such an approximation can be obtained from line source theory (Gilbert and Knopoff, 1961).

A general reflection coefficient, $\mathfrak{R}(p)$, can always be written in the following form

$$\mathfrak{R}(p) = (A(p) - \eta_m B(p))/(A'(p) + \eta_m B'(p))$$

where A's and B's are real constants when $p = 1/c_m$. With this form of $\mathfrak{R}(p)$

$$\frac{d\psi}{dt} \approx \frac{p}{\eta_m}\left(\frac{AB' + A'B}{A'^2}\right)\frac{\sqrt{p}}{\eta_1}\left(\frac{dp}{d\tau}\right)^2 \mathfrak{J}(p)$$

where

$$\eta_m \approx \left(\frac{2}{c_m}\left(\frac{dp}{d\tau}\right)(t - t_p)\right)^{1/2}.$$

The convolution process yields

$$\frac{1}{\sqrt{t}} * (t - t_p)^{1/2} = \pi H(t - t_p).$$

Substituting these approximations into (A14) we obtain the initial behavior of P-head wave arrival

$$P(r, z, t) = \left(\frac{AB' + A'B}{A'^2}\right)\left(\frac{p\mathfrak{J}(p)}{\eta_1(rL^3)^{1/2}}\right)H(t - t_p) \tag{A16}$$

where

$$L = \frac{dt}{dp} = r - 2pTh_j/\eta_j.$$

L can be interpreted as the distance traveled in the refractor. The A's and B's are:

$$A = -p^2(k_r - p^2)^2 + \eta_n\eta_m'(k_m - p^2)^2 - k_nk_m\eta_n\eta_m'$$

$$A' = p^2(k_r - p^2)^2 + \eta_n\eta_n'(k_m - p^2)^2 - k_nk_m\eta_n\eta_m'$$

$$B = -\eta_n\eta_n'\eta_m'p^2 + \eta_m'(k_n - p^2)^2 - \eta_n'k_nk_m$$

$$B' = \eta_n\eta_n'\eta_m'p^2 + \eta_m'(k_n - p^2)^2 - \eta_n'k_nk_m$$

$$k_n = -\tfrac{1}{2}(\rho_n/(\mu_m - \mu_n)), \qquad k_m = \tfrac{1}{2}(\rho_m/(\mu_m - \mu_n))$$

$$k_r = k_n + k_m.$$

The refracted wave generated at a solid/solid interface has been studied by Heelan (1953). Our first motion approximation agrees with his results.

First Motion at Reflection

The high-frequency solution assuming a step function source can be written

$$P(r, z, t) = \sqrt{\frac{2}{r}}\frac{1}{\pi}\frac{1}{\sqrt{t}} * \left[\mathscr{I}\mathrm{m}\frac{\sqrt{p}}{\eta_1}\,\mathcal{R}(p)\mathfrak{I}(p)\frac{dp}{d\tau}\right]. \tag{A17}$$

In the first-motion approximation only values of p near p_0 influence the behavior of $P(t)$. The only function that is not slowly varying near p_0 is $(dp/d\tau)$. Thus we need to express $(dp/d\tau)$ as a function of t and perform the convolution assuming $p = p_0$ in all other functions.

We expand t in a power series about the point t_R, that t which makes $(dp/d\tau) = 0$.

$$t = t_R + \frac{dt}{dp}(p - p_0) + \frac{d^2t}{dp^2}(p - p_0)^2 \cdots$$

to first order

$$t - t_R = \frac{1}{2}\left(\frac{d^2t}{dp^2}\right)(p - p_0)^2$$

solving for p and taking the derivative

$$\frac{dp}{dt} \approx (t - t_R)^{-1/2} \Big/ \left(2\frac{d^2t}{dp^2}\right)^{1/2}_{p=p_0} \tag{A18}$$

Next, d^2t/dp^2 must be evaluated

$$t = pr + \sum 2Th_j\eta_j$$

and taking the derivative

$$\frac{dt}{dp} = r - 2\sum Th_j\,p/\eta_j$$

and

$$\frac{d^2t}{d^2p} = -2\sum Th_j/\eta_j^3c_j^2. \tag{A19}$$

Substituting (A19) into (A18) into (A17) yields

$$P(r, z, t) = \sqrt{\frac{2}{r}}\frac{1}{\pi}\,\mathscr{I}\mathrm{m}\left[\frac{\sqrt{p}}{\eta_1}\,\mathcal{R}(p)\mathfrak{I}(p)\left(-2\sum\frac{2Th_j}{\eta_j^3c_j^2}\right)^{-1/2}\right].(t - t_R)^{-1/2} * (t)^{-1/2}.$$

Performing the convolution the equation reduces to

$$P(r,z,t) = \mathfrak{J}(p)\sqrt{\frac{p}{r}}\frac{1}{\eta_1}\left(\sum\frac{2Th_j}{\eta_j^3 c_j^2}\right)^{-1/2}\cdot\left\{\mathcal{R}e(\mathcal{R}(p))H(t - t_R) - \frac{\mathcal{I}m(\mathcal{R}(p))}{\pi}\operatorname{Log}\left(\frac{|t_R - t|}{2t_R}\right)\right\}$$

where all functions of p are to be evaluated at $p = p_0$.

Transition Layer

Here the formulation will be expanded to include a sandwiched layer. The only added complexity is the possibility of mode change at each interface. Again the method of generalized transmission and reflection coefficients applies and the solution becomes

$$P(r, z, t) = \sum P_n(r, z, t)$$

where

$$\bar{P}_n(r, z, s) = \frac{-i}{\pi}\int_\Gamma K_0(spr)f_n(p)\,\frac{p}{\eta_1}\,e^{-sg_n(p)}dp.$$

The function g_n describes the generalized ray path and f_n is the product of all reflections and transmissions associated with this particular ray.

We assume the same problem setup as that in the last section except the bottom layer is considered thin. The solution is carried down to this layer and back as before. The procedure followed is to sum up rays until their amplitudes become negligible and/or arrive late. The first set of rays considered suffers no internal reflections. They are:

$$PP,\ PS,\ SP,\ SS$$

where P and S indicate crossing layer k in the P-mode and S-mode respectively. k is the index of the thin layer; j is the layer above and l is the layer below. The second set of ravs contains one internal reflection and is

$$\begin{array}{cccc} PPPP & PSPP & SPPP & SSPP \\ PPPS & PSPS & SPPS & SSPS \\ PPSP & PSSP & SPSP & SSSP \\ PPSS & PSSS & SPSS & SSSS. \end{array}$$

A number of these rays have the same time and magnitude which will be referred to as the same response. This allows some simplification in the summation procedure. Two basic symmetrics exist:

$$T_{P_jP_k}\mathcal{R}_{P_kS_l}T_{S_kP_j} = T_{P_jS_k}\mathcal{R}_{S_kP_l}T_{P_kP_j}$$

$$\mathcal{R}_{P_kS_l}\mathcal{R}_{S_kP_j} = \mathcal{R}_{P_kS_j}\mathcal{R}_{S_kP_l} .$$

The proof of these two statements is easily accomplished by applying the explicit coefficients. In the first set

$$PS = SP$$

and we require three responses. In the second set:

$$PPPS = SPPP$$

$$PPSP = PSPP$$

$$PPSS = SSPP$$

$$PSPS = SPSP$$

$$PSSS = SSSP$$

$$SPSS = SSPS$$

which reduces to ten responses. It is found in working with wide angle reflections that coefficients involving shear transmissions decrease very rapidly and seldom is it necessary to include the second set. We include them mostly for completeness although it is necessary to show that they are negligible by calculation.

We adopt the following notation:

L_{PS} = transmission into layer as shear mode
L_{PP} = transmission into layer as primary mode
K_{PP} = transmission back up as primary mode
K_{SP} = transmission back up as shear mode
M_{PP} = no. of PP internal reflections at the top
M_{SP} = no. of SP internal reflections at the top
M_{PS} = no. of PS internal reflections at the top
M_{SS} = no. of SS internal reflections at the top
N_{PP} = no. of PP reflections at the bottom
N_{SP} = no. of SP reflections at the bottom
N_{PS} = no. of PS reflections at the bottom
N_{SS} = no. of SS reflections at the bottom
L_{ts} = crossing in S-mode.
L_{tp} = crossing in P-mode.

Next we apply an index n to each of these constants and let this index indicate each response

$$n = 1 \rightarrow PP$$

$$n = 2 \rightarrow PS$$

$$n = 3 \rightarrow SS$$

etc.

With these definitions g_n and f_n can be written

$$g_n(p) = 2\sum_{m=1}^{j} Th_m\eta_n + L_{ts}\cdot\eta_k' Th_k + L_{tp}\cdot\eta_k Th_k$$

$$f_n(p) = \mathfrak{I}(p)\cdot(\mathfrak{R}_{P_kP_j})^{M_{PP}}\cdot(\mathfrak{R}_{P_kS_j})^{M_{PS}}\cdot(\mathfrak{R}_{P_kP_l})^{N_{PP}}\cdot(\mathfrak{R}_{P_kS_l})^{N_{PS}}\cdot(\mathfrak{R}_{S_kP_j})^{M_{SP}}$$

$$\cdot(\mathfrak{R}_{S_kS_j})^{M_{SS}}\cdot(\mathfrak{R}_{S_kP_l})^{N_{SP}}\cdot(\mathfrak{R}_{S_kS_l})^{N_{SS}}\cdot(T_{P_jP_k})^{L_{PP}}\cdot(T_{P_jS_k})^{L_{PS}}\cdot(T_{P_kP_j})^{K_{PP}}\cdot(T_{S_kP_j})^{K_{SP}}.$$

The numerical solution is now easily accomplished by applying the recipe. Explicit forms for the transmission and reflection coefficients are given below:

$$\mathfrak{R}_{P_iP_j} = (-Q_1 + Q_2 + Q_3 - Q_4 - Q_5 + Q_6)/D$$

$$\mathfrak{R}_{P_iS_j} = 2p\eta_i[(k_j - p^2)(k_r - p^2) - \eta_j\eta_j'(k_i - p^2)]/D$$

$$T_{P_iP_j} = 2k_i\eta_i[\eta_j'(k_i - p^2) - \eta_i'(k_j - p^2)]/D$$

$$T_{P_iS_j} = 2k_ip\eta_i[\eta_i'\eta_j - (k_r - p^2)]/D$$

$$\mathfrak{R}_{S_iS_j} = (-Q_1 + Q_2 + Q_3 - Q_4 + Q_5 - Q_6)/D$$

$$\mathfrak{R}_{S_iP_j} = (-2p\eta_i'((k_j - p^2)(k_r - p^2) - \eta_j\eta_j'(k_i - p^2))/D$$

$$T_{S_iS_j} = -2k_i\eta_i'(\eta_i(k_j - p^2) - \eta_j(k_i - p^2))/D$$

$$T_{S_iP_j} = 2k_ip\eta_i'((k_r - p^2) - \eta_i\eta_j')/D$$

where

$$Q_1 = p^2(k_r - p^2)^2 \qquad Q_4 = \eta_j\eta_j'(k_i - p^2)^2$$

$$Q_2 = \eta_i\eta_j\eta_i'\eta_j'p^2 \qquad Q_5 = \eta_i\eta_j'k_ik_j$$

$$Q_3 = \eta_i\eta_i'(k_j - p^2)^2 \qquad Q_6 = \eta_j\eta_i'k_ik_j$$

and

$$D = Q_1 + Q_2 + Q_3 + Q_4 - Q_5 - Q_6 .$$

The coefficients starting with index P reduce to those given by Muskat and Meres (1940) after substituting $p = \sin \theta / c_i$ where θ is the angle of incidence. Replacing p by $\sin \theta / s_1$, in the coefficients starting with index S produces, likewise, the plane wave coefficients discussed by Muskat and Meres.

The case of two sandwiched layers is solved in the same fashion. The details are given by Helmberger (1967).

Acknowledgments

I wish to thank Dr. Russell Raitt and Dr. Freeman Gilbert for their guidance and encouragement throughout this work. This research was supported in part by the Air Force Office of Scientific Research and the Marine Physical Laboratory under Office of Naval Research sponsorship.

References

Arons, A. (1948). Secondary pressure pulses due to gas glove oscillation in underwater explosives. *J. Acoust. Soc Amer.* **20,** 277–282.

Arons, A. (1954). Explosive shock wave parameters at large distances from the charge. *J. Acoust. Soc. Amer.* **26,** 343–346.

Cagniard, L. (1939). *Reflexion et Refraction des ondes Seismiques Progressives.* Gauthier-Villars, Paris.

Cagniard, L. (1962). *Reflection and Refraction of Progressive Seismic Waves.* Translated by Dr. Edward A. Flinn, McGraw-Hill, New York.

Cerveny, V. (1965). Features of reflected and head waves in the region of initial points. *IZV. Earth Physics Series,* **8,** 518–522.

Dix, C. (1954). The method of Cagniard in seismic pulse problems. *Geophysics,* **19,** 722–738.

Donato, R. (1964). Amplitude of *P*-head waves. *J. Acoust. Soc. Amer.* **36,** 19–25.

Gilbert, F. (1963). Transient response of a fluid-solid interface due to an impulsive pressure-point source. *Office of the director of Defenses, Bulletin* **32.**

Gilbert, F. and L. Knopoff (1961). The directivity problem for a buried line source. *Geophysics,* **26,** 626–634.

Heelan, P. (1953). On the theory of head waves. *Geophysics,* **18,** 871–893.

Helmberger, D. (1967). Head waves from the Oceanic Mohorovivic Discontinuity. *Thesis, UCSD,* La Jolla, California.

Hoop, A. de (1960). A modification of Cagniard method for solving seismic pulse problems. *Appl. Sci. Res. B,* **8,** 349–356.

Jeffreys, H. (1926). On compressional waves in two superposed layers. *Proc. Cambridge Phil. Soc.* **23,** 472–481.

Knopoff, L., F. Gilbert, and W. Pilant (1960). Wave propagation in a simple layer. *J. Geophys. Res.* **65,** 265–278.

Lamb, H. (1904). On the propagation of tremors over the surface of an elastic solid. *Phil. Trans. Roy. Soc. (London),* **A203,** 1–42.

Muskat, M., and M. Meres (1940). Reflection and transmission coefficients for plane waves in elastic media. *Geophysics,* **5,** 115–148.

Pekeris, C., Z. Alterman, F. Abramovici, and H. Jarosch (1965). Propagation of a compressional pulse in a layered solid. *Reviews of Geophysics,* **3,** 25–47.

Phinney, R. (1961). Propagation of leaking interface waves. *Bull. Seism. Soc. Amer.* **51,** 527–555.

Raitt, R. (1952). *Oceanographic Instrumentation,* N.A.A. - N.R.C. Publ. 309, 70.

Shor, G. Jr. (1963). Refraction and reflection techniques and procedures. *The Sea*, Vol. 3, 20–38.

Shor, G. Jr. (1964). Structure of the Bering Sea and the Aleutian Ridge. *Marine Geol.*, **1**, 213–219.

Spencer, T. (1960). The method of generalized reflection and transmission coefficients. *Geophysics*, **25**, 625–641.

Spencer, T. (1965). Refraction along a layer. *Geophysics*, **30**, 369–388.

Strick, E. (1959). Propagation of elastic wave motion from an impulsive source along a fluid/solid interface, II. Theoretical pressure pulse. *Phil. Trans. Roy. Soc.* (*London*), **A251**, 465–523.

Tulina, Y. (1965). A comparison between magnetic anomalies and the seismic properties of the Mohorovicic Discontinuity. (AZV). *Acad. Sci. USSR, Physics of the Solid Earth*, **3**, 170–176.

Weston, D. (1960). Underwater explosives as acoustic sources. *Proc. Phys. Soc.*, **76**, 233–249.

Weyl, H. (1919). Ausbreitung elektromagnetischer Wellen. *Ann. der Phys.*, **60**, 481–500.

Scripps Institute of Oceanography
University of California
San Diego, California

Manuscript received June 19, 1967.